

NiTi-Enabled Composite Design for Exceptional Performances

Yang Shao¹ · Fangmin Guo¹ · Yang Ren³ · Junsong Zhang² · Hong Yang² ·
Daqiang Jiang¹ · Shijie Hao¹ · Lishan Cui¹

Published online: 8 March 2017
© ASM International 2017

Abstract In an effort to further develop shape memory alloys (SMAs) for functional applications, much focus has been given in recent years to design and create innovative forms of SMAs, such as functionally graded SMAs, architecture SMAs, and SMA-based metallic composites. This paper reports on the progress in creating NiTi-based composites of exceptional properties stimulated by the recent discovery of the principle of lattice strain matching between the SMA matrix and superelastic nanoinclusions embedded in the matrix. Based on this principle, different SMA–metal composites have been designed to achieve extraordinary shape memory performances, such as complete pseudoelastic behavior at as low as 77 K and stress plateau as high as 1600 MPa, and exceptional mechanical properties, such as tensile strength as high as 2000 MPa and Young’s modulus as low as 28 GPa. Details are given for a NiTi–W micro-fiber composite prepared by melt infiltration, hot pressing, forging, and cold rolling. The composite contained 63% in volume of W micro-fibers of ~0.6 μm thickness. In situ synchrotron X-ray diffraction revealed that the NiTi matrix underwent martensite transformation during tensile deformation while the W micro-fiber deformed elastically with a maximum strain of 0.83%

in the loading direction, implying a W fiber stress of 3280 MPa. The composite showed a maximum high tensile strength of 2300 MPa.

Keywords Shape memory alloy · Martensite transformation · Composite · Nanowires

Introduction

Shape memory alloys (SMAs) are a group of metallic materials of unique properties that are unmatched by conventional metal alloys. These unique properties include the shape memory effect and pseudoelasticity (superelasticity). By shape memory effect, the alloy can be deformed well beyond its elastic limit and then be recovered to its original shape upon heating at a later stage. In doing so it outputs a mechanical work. In pseudoelasticity, the alloy is able to recover its original shape spontaneously upon unloading, performing a mechanical work to the environment. These shape recovery and mechanical work outputs have enabled SMAs to be widely used in many functional applications.

In recent years, much effort has been made to design novel structured SMAs to further extend their functional properties. To achieve this, three main strategies have been taken. The first is to develop architected shape memory materials. These materials combine the advantages of the exceptional properties of shape memory alloys and the unique characteristics of the physical forms of materials. The most common example is porous shape memory alloys (or shape memory foams) [1–3]. These materials may be designed to have tailored levels of compliance and enlarged superelastic deformation ranges. Another example is the shape memory alloy honeycomb structures [4–6]. Similar to that, Favier et al. tested the mechanical behavior

✉ Lishan Cui
lishancui63@126.com

¹ State Key Laboratory of Heavy Oil Processing and Department of Materials Science and Engineering, China University of Petroleum, Beijing 102249, China

² School of Mechanical and Chemical Engineering, The University of Western Australia, Crawley, WA 6009, Australia

³ X-ray Science Division, Argonne National Laboratory, Argonne, IL 60439, USA

of stacked NiTi tubular structures [7]. Architected shape memory materials also include woven textiles and nitinol stents [8–10]. Also in this concept are shape memory springs as the earliest examples.

The second strategy is to create functionally graded shape memory alloys. Such a material may exhibit property variation through its length or thickness, via either a gradient change of the microstructure or a gradient change of the chemical composition. Mahmud et al. designed functionally graded NiTi alloys by annealing cold-worked NiTi wires within a temperature gradient field [11–13]. These materials exhibit a progressive stress-induced martensitic transformation for better controllability for actuator applications. Meng et al. designed and created 2D functionally graded NiTi thin plates with property gradient through the thickness [14–18]. These materials exhibit a unique back-and-forth 4-way shape memory effect upon a single heating or cooling in a “fishtail-like” manner.

The third strategy is to develop SMA–metal nanocomposites. Many designs have been developed in the past, including SMA–ceramic composites [19–22], SMA–polymer composites [23–25], and SMA–metal matrix composites [26–30]. In ceramic matrix composites, SMAs are added mostly in particular forms with the objective to improve composite toughness and strength. In polymer-based composites, SMAs are most added as aligned wires or woven structures to alter and control the mechanical properties of the composites, such as stiffness and vibration damping [31], or to morph the shape [32]. Most of the metal matrix-SMA composites use low melting temperature metals as the matrix, such as Al, Sn, and Mg [19–22]. In all these composites, the primary purpose is to use SMA to enhance strength, toughness, or to add temperature response ability to the composites.

However, much more interest has been stimulated in the recent few years by a new type metal-based NiTi–X nanocomposites [33–37]. This is based on a breakthrough discovery of the unique ability of NiTi as the composite matrix in inducing ultra-large elastic strains (e.g., above 5%) in the nanometallic inclusions embedded in the composites. This is enabled by the mechanism of “lattice strain matching” between the uniform lattice distortion of the martensitic transformation of the NiTi matrix and the uniform elastic deformation of the nanoinclusions [33]. Ultra-large elastic strains imply ultra-high strength thus the possibility to create super strong composite materials. In addition, ultra-large elastic strains in solids also have the potential to change the interatomic bonding conditions and electron states within the solid, thus potential to alter its many functional and chemical properties [38]. This has become an emerging frontier study in the field of materials science referred to as the “elastic strain engineering” [39–41]. In this regard, this new SMA–X metal matrix

composite has the potential to be a game changer by (i) creating shape memory materials of superior performances and (ii) enabling other materials to exhibit improved or unprecedented functional properties.

In this paper, we present our recent progress in the study on “lattice strain matching” to enable NiTi–metal nanocomposites, including the design concept, design objectives, and the fabrication methods of these materials. A novel NiTi–W micro-fiber composite is explored based on this design concept.

Shape Memory Alloy Composite Design Concept

SMA matrix composites offer unique opportunities which other composite matrices may not, in two aspects, macroscopic and microscopic features.

Macroscopic Features

Macroscopically, the stress–strain behavior of SMAs is distinctively different from that of conventional elastic–plastic metals, due to their martensitic transformation. The stress–strain curve of a SMA can be divided into four stages (Fig. 1, the red curve), including (i) elastic deformation, (ii) stress-induced martensitic transformation or martensite reorientation over stress plateau, (iii) the elastic deformation of the orientated martensite, and (iv) plastic deformation. This is in clear contrast to the two-stage elastic–plastic deformation behavior of a

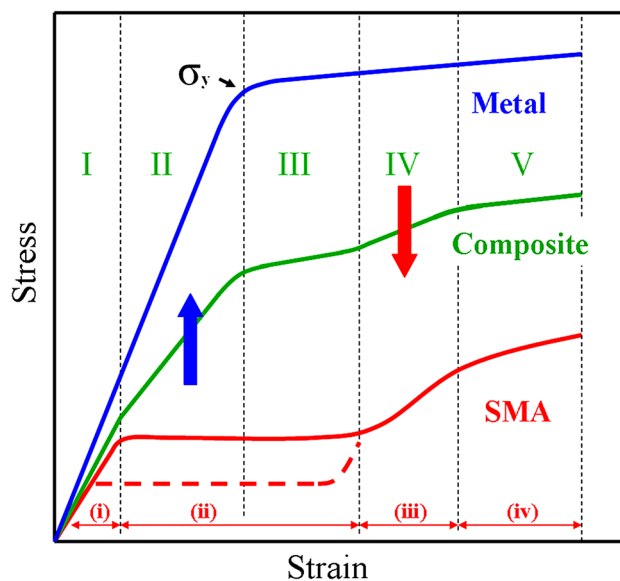


Fig. 1 Schematic illustration of the different macroscopic mechanical behaviors of a shape memory alloy and a conventional elastic–plastic metal, the internal load transfer within the dual-phase composites, and expected mechanical response of the composite

conventional metal (Fig. 1, the blue curve). When forming into a composite, different internal load transfer processes may be expected [42, 43]. Based on the way of internal sharing and transfer of the applied load, the deformation behavior of the composite may be divided into five stages, as indicated in Fig. 1a. In stage I, when both the SMA matrix and the conventional metal inclusion are in elastic state, normal load sharing by the principle of volume fraction, Young's moduli of the two phases, and their configuration (in series or parallel connection) may be expected. Processing to stage II, when the SMA is exhibiting complete compliance over the stress plateau, load is transferred to the metal inclusion (as indicated by the blue arrow), which is still in the elastic stage. In stage III when both components are in high compliance state, normal sharing of the applied load occurs. Continuing deformation into stage IV, when the SMA matrix stiffens after the martensitic transformation (or martensite reorientation), reverse load transfer from the more compliant, plastically deforming metal inclusion to the SMA matrix occurs, as indicated by the red arrow. Such complex internal load sharing process leads to new and complex macroscopic deformation behavior of the composites, as schematically expressed by the green curve.

From the above description, it is easy to see that SMAs offer a unique opportunity for composite design. It is also clear that by altering some parameters, e.g., the yielding point of the metal inclusion (e.g., using nanomaterials that show extraordinarily high yield strength and elastic limit) and the stress plateau length of the SMA matrix (using different shape memory alloys), different macroscopic stress–strain behaviors may be created, providing versatility for designing SMA–M composites of innovative performances.

Microscopic Features

SMAs also differ from conventional metals in deformation at the microscopic scale. A SMA deforms via stress-induced martensitic transformation or stress-assisted martensite reorientation, whereas a conventional elastic–plastic metal deforms plastically via dislocation slipping at atomic scale after passing the elastic limit. These two mechanisms are fundamentally different at the crystal lattice scale, with the martensitic transformation being uniform in lattice distortion, whereas dislocation slip being highly localized at the lattice level. In comparison, elastic deformation of solids is also a uniform lattice distortion. For free-standing nanowires, the elastic strain limits have been shown to be generally 4–7% [44–47]. For SMAs, the tensile strain of the martensitic transformation is typically

5–8% [48, 49], a good match with those of nanomaterials. On the other hand, the elastic strains at the yield point of conventional metals are typically below 0.5% and at a dislocation line, the lattice distortion is very high (100% in principle) [33, 50], a far mismatch of lattice distortion with nanowires.

This concept is schematically illustrated in Fig. 2. Figure 2a expresses the situation of a conventional metal matrix–nanowire composite. The matrix deforms via dislocation slip, and the dislocations at the matrix–nanowire interface present high mismatch in lattice distortion between the two components. This mismatch between the non-uniform plastic deformation and the uniform elastic strain of the nanowires prevents effective load transfer across the interface from the matrix to the nanowire. When designing metallic matrix composites containing nanowires, which are expected to exhibit ultra-large elastic strains for high strengths, such designs are clearly ineffective [44–47, 51].

Figure 2b expresses the situation of a SMA matrix–nanowire composite. The matrix deforms via stress-induced martensitic transformation, which produces a uniform lattice strain of 5–7%, which is a good match with the expected large elastic strains of the nanowire, preserving the integrity of the interface. In this regard, it is clear that all the atoms in the martensite region contribute effectively to load transfer from the matrix to the nanowire, leading to ultra-large elastic deformation of the nanowire and extraordinary strength of the composite. This novel materials design concept is referred to as “lattice strain matching” and “collective atomic load transfer” [33].

Much success has been achieved using this principle. Hao et al. designed in situ Nb nanowire-reinforced NiTi SMA composite, which exhibited a large quasi-linear elastic strain of over 6%, a low Young's modulus of ~ 28 GPa, and a high yield strength of minimum 1.65 GPa [33]. Zhang et al. designed nacre-like structure of NiTi–Ti₃Sn nanolamellar composite, which showed a compressive strength of 3000 MPa [52]. In this regard, it is clear that the unique microscopic feature at the crystal lattice level of SMAs offers another unprecedented opportunity for composite design.

Design Objectives of SMA Composites

SMA nanocomposites may be designed to achieve different objectives, largely (i) to improve and enhance shape memory properties, (ii) to form super composites of extraordinary mechanical properties, and (iii) to use shape memory alloys as an enabler to induce new and extraordinary properties of other materials, for example, via the principle of elastic strain engineering [38].

To Improve and Enhance Shape Memory Properties

One example of modifying the intrinsic mechanical behavior of NiTi shape memory alloys is to create large quasi-linear superelasticity of high strength and large stress window for better actuation control. Figure 3 shows schematically this strategy. In Fig. 3a, the rigid component represents the high-strength nanowires. The green curve represents the stress–strain behavior of the composite. It is seen that upon deformation to the end of the stress plateau of the SMA, the nanowire component has undergone some plastic deformation. At the end of the first deformation cycle, the plastically deformed nanowires endure a compressive stress (as indicated by the blue dot), whereas the SMA matrix endures a tensile residual stress (indicated by the red dot). In the subsequent tensile cycle (Fig. 3b), the stress-induced martensitic transformation commences at a lower stress, due to the pre-existing internal tensile stress in

the SMA matrix and propagates in a manner with progressively increasing stress. Meanwhile, the nanowires deform elastically. Thus, a quasi-linear superelastic behavior with a small hysteresis is created.

Following this design concept, an in situ Nb nanowire-reinforced NiTi composite was fabricated via NiTi–Nb pseudoeutectic solidification and wire drawing. Figure 4a shows the microstructure of the in situ composite wire. The microstructure consists of a high density of Nb nanowires of a mean diameter of 60 nm well dispersed and well aligned in the NiTi matrix along the wire axial direction. Figure 4b shows a stress–strain curve of a tensile deformation of the composite wire, after a pre-deformation to 9.5%. The nanocomposite exhibited a large quasi-linear elastic strain of 5.3%, a low apparent elastic modulus of ~ 27 GPa, and a high yield strength above 1.56 GPa. The relative hysteretic energy loss of the quasi-linear superelastic behavior is 18.1% (or the energy efficiency of the

Fig. 2 Schematic of lattice strain matching at the matrix–nanowire interface inside a composite. **a** Situation of the elastic–plastic metal matrix composite, where high lattice distortion mismatch occurs at the interface; **b** situation of SMA–metal matrix composite, where near perfect lattice strain matching occurs at the interface

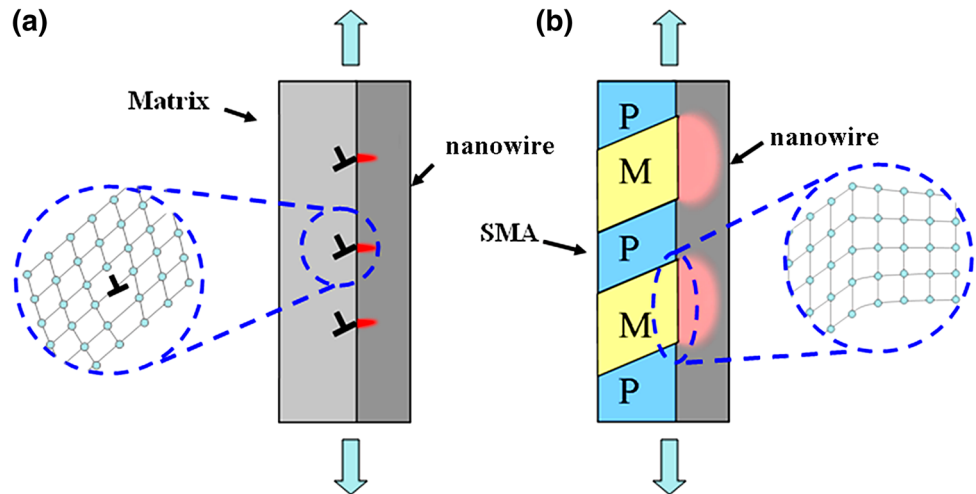
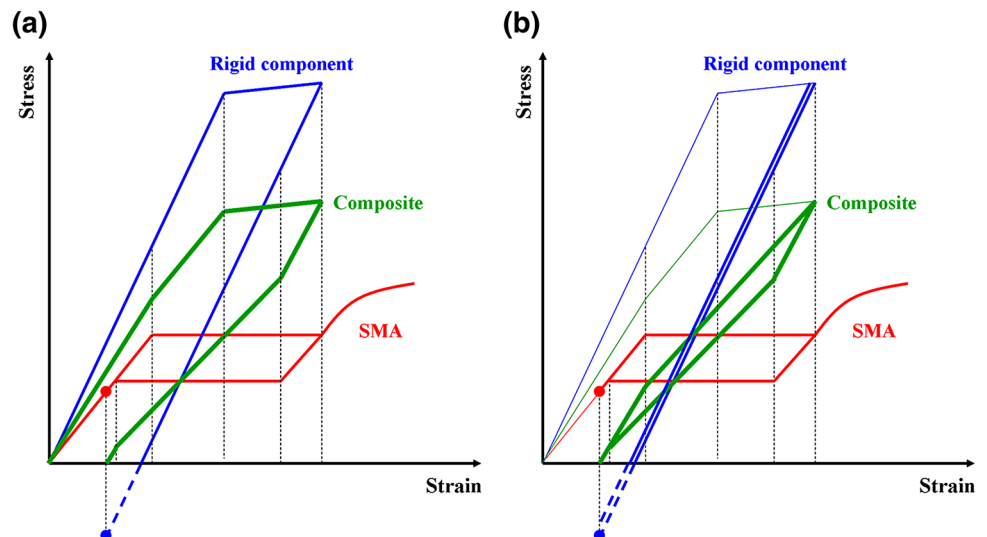


Fig. 3 Schematics of large linear elastic deformation in tensile loading cycles of SMA nanocomposite. **a** The first tensile deformation cycle; **b** The second loading cycle



quasi-linear superelastic behavior is 81.9%). In this in situ NiTi–Nb nanowire composite, synchrotron X-ray diffraction analysis has confirmed that after one tensile deformation cycle to 9.5%, the NiTi matrix had a tensile residual strain of 1% and the Nb nanowires had a residual compressive strain of $-1.4%$, confirming the design concept derived from the above analysis. Upon the second deformation cycle, the Nb nanowires experienced an ultra-large elastic strain of $4.2\% - (-1.4\%) = 5.6%$, which matches well with the phase transformation strain of $\sim 7%$ of the NiTi matrix [33].

Figure 5 shows another situation where the shape memory property of a SMA can be enhanced. The composite exhibits pseudoelasticity of high plateau stress and small hysteretic hysteresis using high-strength nanowire reinforcement. The original strength of the NiTi matrix can also be tailored by adjusting the inter-nanowire spacing, as expressed in Fig. 5. Smaller spacing between nanowires (the right case) helps forming nanocrystalline structure of the NiTi matrix by limiting grain growth during heat treatment, which could effectively suppress the martensite transformation and increase the plateau stress of the NiTi

Fig. 4 An in situ NiTi–Nb nanowires composite prepared by NiTi–Nb pseudoeutectic solidification and wire drawing. **a** Microstructure of the in situ composite wire revealing well aligned and dispersed Nb nanowires within a continuous NiTi matrix. The main micrograph shows the longitudinal microstructure and the inset shows the transverse microstructure. **b** A quasi-linear superelastic tensile stress–strain curve at room temperature of the composite after a pre-tensile deformation of 9.5%

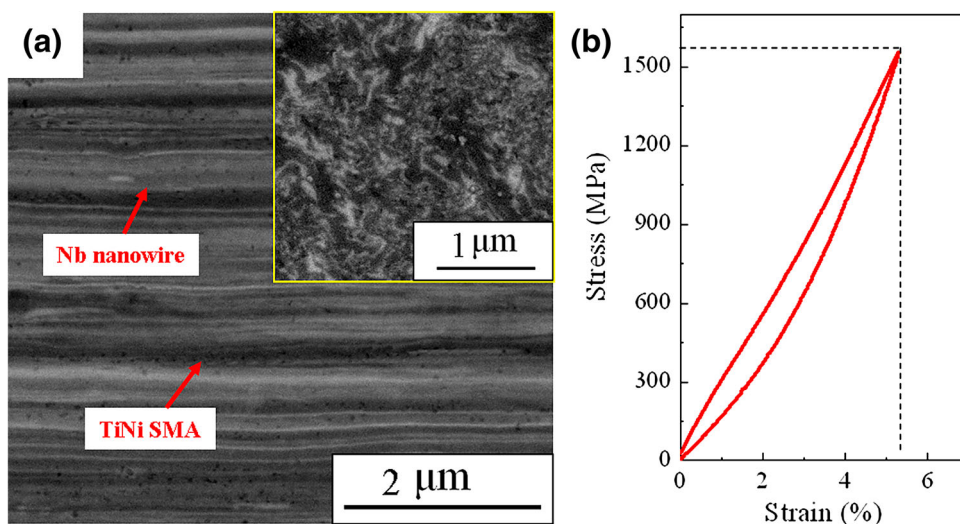


Fig. 5 Schematics of high strength, low hysteresis pseudoelasticity of SMA nanocomposite

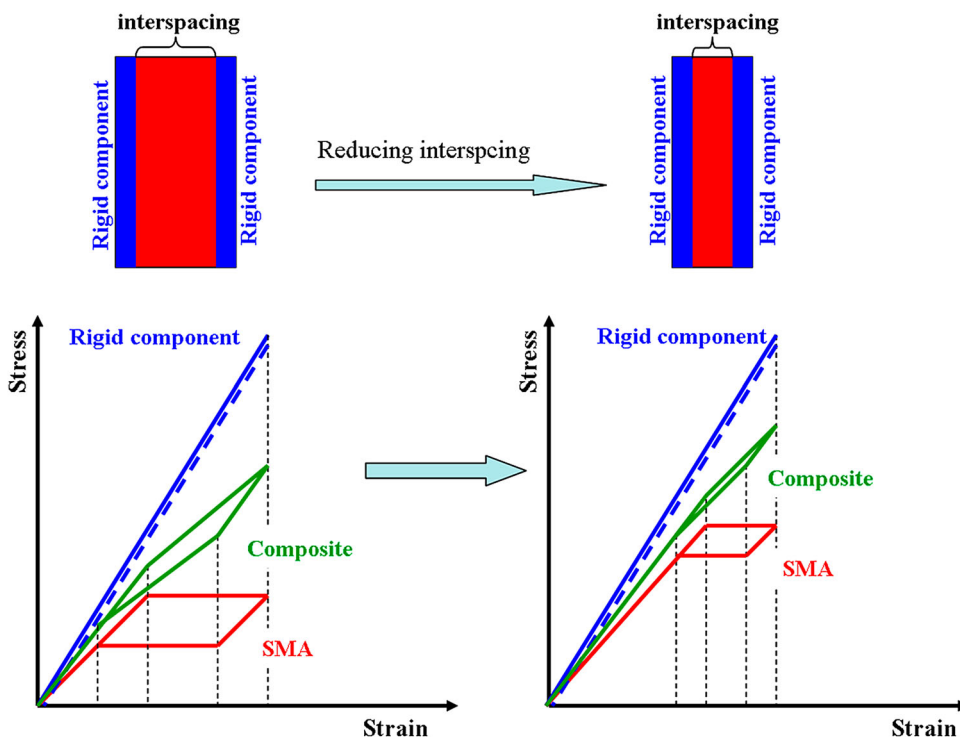
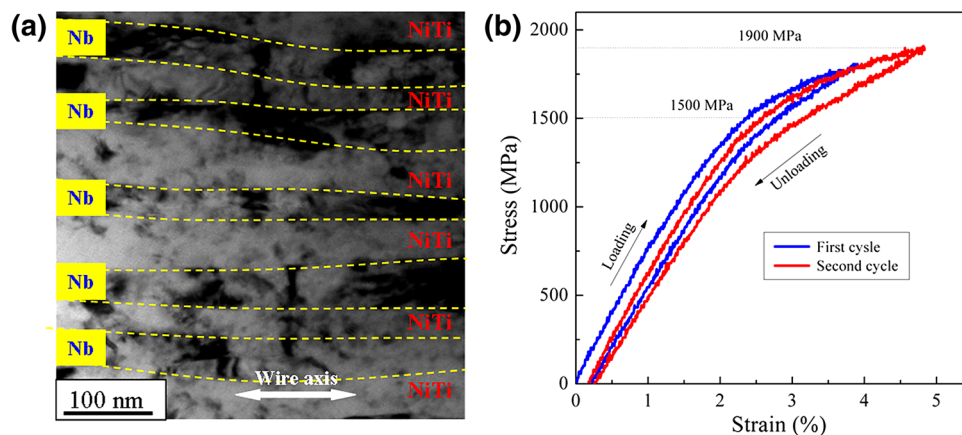


Fig. 6 Microstructure and mechanical properties of a nanocrystalline NiTi–Nb nanowire composite. **a** Transmission electron micrograph of the longitudinal structure of the composite wire; **b** tensile stress–strain behavior of the composite



matrix during tensile loading. Meanwhile, smaller inter-nanowire spacing could effectively reduce the phase interfacial movement distance in nanocrystalline NiTi matrix, which leads to the reduction of transformation hysteresis [53, 54].

This design principle has been applied to fabricate nanostructured NiTi matrix–Nb nanowire composite. Figure 6a shows the microstructure of the composite. The microstructure consists of Nb nanowires of ~ 30 nm in diameter with a mean spacing of 45 nm. The NiTi matrix is nanocrystalline, with an average grain size of 15 nm. Figure 6b shows the tensile stress–strain curve of the composite wire. The composite wire has a high pseudoelastic stress plateau of 1.5–2.0 GPa and a small stress hysteresis of about 100 MPa. This pseudoelastic strength is about three times of that of general commercial NiTi shape memory alloys [55]. The stress hysteresis is also significantly smaller than those of common commercial NiTi alloys (~ 320 MPa [55]).

To Create Super Composites of Exceptional Mechanical Properties

When the volume fraction of the nanoreinforcement phase is further increased, the SMA nanocomposite will lose the macroscopic mechanical features of shape recovery as seen in SMAs. The small volume fraction of the SMA in such SMA nanocomposites acts more like a metallic bonder and load distributor, as per the “collective atomic load transfer” principle, and the high-strength nanoreinforcement is the main load bearer and material function provider. In addition, the relatively low flow stress and large flow strain associated with the martensitic transformation help further to distribute the internal load more uniformly at the macroscopic scale, may contribute further to the load bearing capability of the composite.

Following this principle, a NiTi–Ti₃Sn lamella composite (and also a NiTi–Ti₅Si₃) inspired by nacre structure

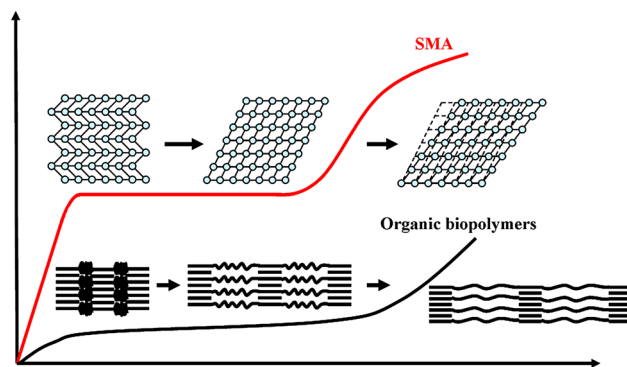


Fig. 7 Comparison of the macroscopic behavior and microscopic mechanism of deformation between SMAs and organic biopolymers

is designed [52, 56]. In nacre, the main load bearing component is aragonite, a biomineral material, bonded together by a soft organic biopolymeric tissue to form a brick-and-mortar structure. In this NiTi–Ti₃Sn lamella composite, the brittle intermetallic Ti₃Sn functions like the brittle aragonite in nacre, and the more compliant NiTi serves as the biopolymer. One significant feature of the biopolymer is the “J-curve”-shaped mechanical behavior, with a low flow stress, large flow strain, and a significant stiffening stage with rapidly increasing stress, as shown in Fig. 7. It is also clear in the figure that NiTi shape memory alloy also exhibits a “J-curve” stress–strain behavior. The low flow stress over a large strain span of the “J-curve” behavior allows easy load redistribution to the brittle and hard component to maximize the load bearing capacity of the composite. The rapidly hardening tail at higher strain levels assures no “run-away” deformation locally to cause pre-mature failure and forces uniform deformation. In addition, NiTi also has a uniform deformation mechanism at crystal lattice scale (Fig. 2b). These characteristics assure both effective load distribution at the macroscopic scale and load transfer at the lattice microscopic level, thus the intrinsic mechanical strength of the nanoreinforcement can be exploited.

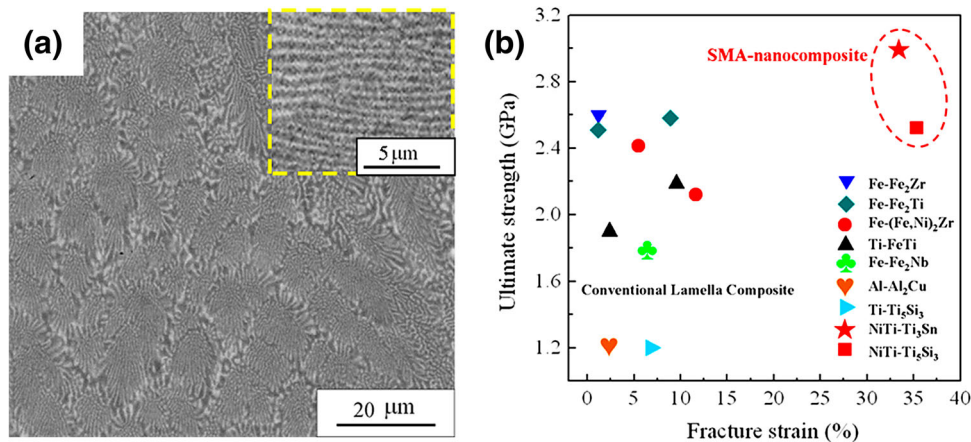


Fig. 8 A NiTi–Ti₃Sn lamella composite fabricated by pseudobinary eutectic casting. **a** Back-scattered SEM microstructure of the NiTi–Ti₃Sn composite. The bright area is Ti₃Sn and the dark area is NiTi. **b** Comparison of the mechanical properties of SMA-enabled NiTi–

Ti₃Sn and NiTi–Ti₅Si₃ composites with other high-performance metal-based lamellar composites in which the soft component is a conventional metal (without the “J-curve” deformation attributes)

The NiTi–Ti₃Sn lamella composite was fabricated by pseudobinary eutectic casting. Figure 8a shows the microstructure of the composite. The composite exhibits a maximum ultimate compressive strength of 3 GPa and a large fracture strain exceeding 30%. Figure 8b shows a comparison of the mechanical properties of the NiTi-based composites (NiTi–Ti₃Sn and NiTi–Ti₅Si₃) with other intermetallic composites containing a soft metal matrix and a hard compound reinforcement. It is apparent that the NiTi-enabled, nacre-like composites are far more superior to all other competitor intermetallic composites.

Configuration Design of SMA Composites

Many novel SMA–metal composites may be fabricated based on the design principles presented above using a shape memory alloy matrix. Figure 9 shows some typical examples of the various internal configurations of SMA composites. The rigid component, or the reinforcement, may be in the forms of particles, aligned nanowires, and nanolamellar or continuous plates. The shape memory alloy matrix may also be provided using different SMAs, e.g., based on consideration of the magnitude of transformation lattice strain, transformation temperature range, and metallurgical conditions for processing (e.g., eutectic casting). To date, in our laboratory, we have fabricated NiTi–Nb nanowire composite [33, 57, 58], TiNiCu–Nb nanowire composite [59], CuZnAl–Mo nanowire composite [34], NiTi–W micro-fiber composite [60], NiTi–Ti₃Sn lamella composite [52], NiTi–Ti₅Si₃ lamella composite [56], and NiTi–W multilayer composite [61].

Fabrication of SMA Composites

In Situ Eutectic Solidification, Ingot Processing, and Wire Drawing

Intermetallic composites may be fabricated either via in situ conversion or additive (ex situ) fabrication. A convenient in situ method for NiTi-enabled intermetallic composites is pseudobinary eutectic casting. This method is based on the principle of high affinity between Ni and Ti in the B2 structure which often functions as one component in a eutectic system. Exemplary pseudobinary NiTi–X eutectic systems include NiTi–Nb [62], NiTi–Ta [63], NiTi–V [64], NiTi–CuTi [65], NiTi–Ti₃Sn [52], and NiTi–Ti₅Si₃ [56]. Figure 10 shows the pseudobinary NiTi–Nb eutectic phase diagram [33].

Such eutectic alloys naturally form well-mixed in situ dual-phase structures, typically in fine lamellar or rod-matrix configurations (e.g., Fig. 10b). Post-ingot processing, e.g., by plate rolling or wire drawing, can convert the two-phase morphology into matrix-nanocomponent structure. Figure 11 shows the processing of in situ NiTi–Nb nanowire composite as an example. The process involves ingot casting, ingot forging or swaging, billet rolling, and finally wire drawing. One obvious advantage of this in situ composite processing route is that it deploys conventional industrial mass production techniques for metal products, thus is of low cost and capable of large quantity production.

Multilayer Folding Plate Rolling

Multilayer folding plate rolling process is another method to produce ex situ SMA composites. SMA plates and other metal plates are firstly stacked alternatively together and

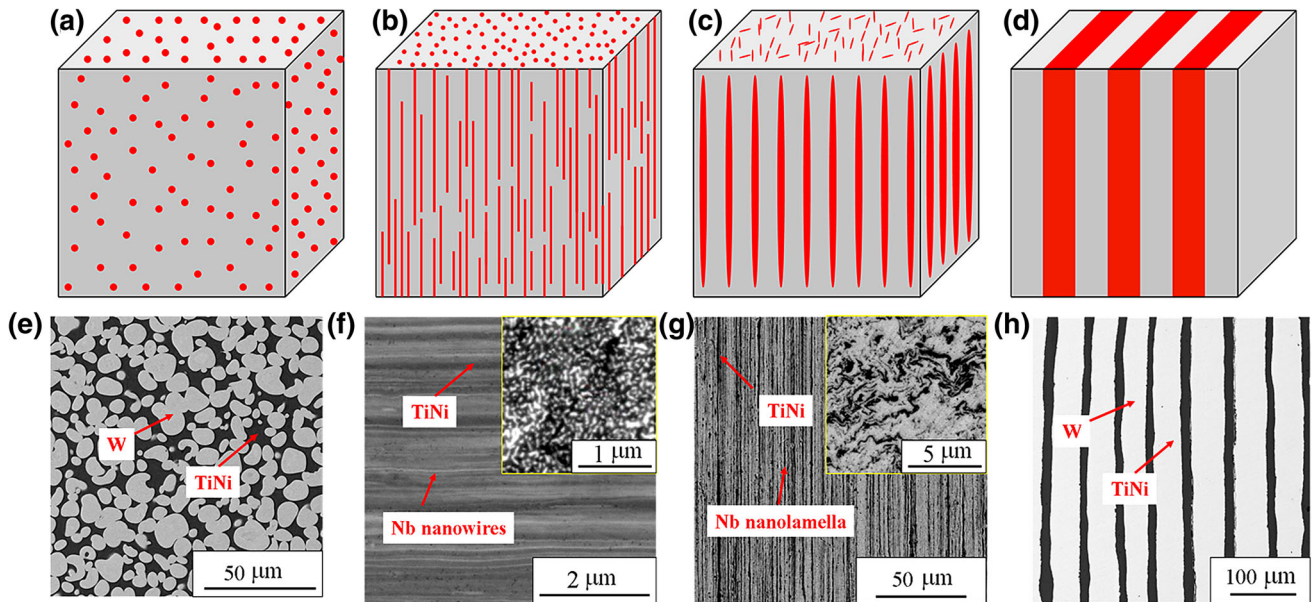


Fig. 9 Schematic illustration of the various types of reinforcement configurations in SMA-enabled nanocomposites: **a** particle reinforcement; **b** nanowire reinforcement; **c** nanolamellae reinforcement; **d** layer/platelet reinforcement (the gray area is SMA matrix, the red area is reinforcement); **e** NiTi–W particulate composite fabricated by

infiltration and hot pressing process; **f** in situ NiTi–Nb nanowire composite fabricated by eutectic casting and wire drawing; **g** NiTi–Nb nanolamella composite; **h** NiTi–W micro-laminated composite fabricated by multilayer folding plate rolling process

Fig. 10 Schematic phase diagram of Nb–NiTi pseudobinary system and the microstructure of $\text{Ti}_{41}\text{Ni}_{39}\text{Nb}_{20}$ as-cast ingot with eutectic composition (the bright area is Nb and the dark area is NiTi)

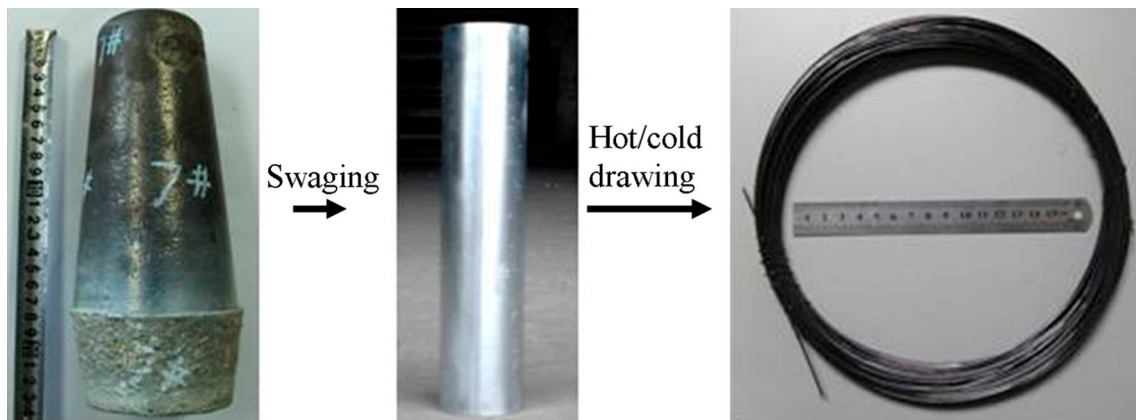
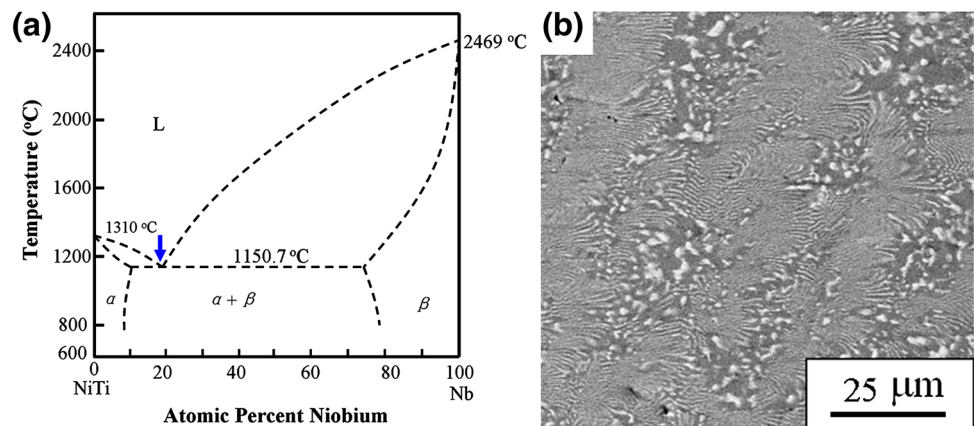


Fig. 11 Typical post-casting ingot processing for producing SMA–nanocomponent composite, as in the case of NiTi–Nb nanowire composite

hot pressed in a vacuum hot pressing furnace. The hot pressed stack was then sealed inside a steel casing and then hot forged/rolled into a thin sheet to reduce thickness of the two components. The rolled sheet may be cut and folded in multiple layers again to form a new stack and rolled again till the component layers are reduced to the desired micrometric or nanometric thicknesses. Using this method, a novel high strength and ductile NiTi–W micro-laminated composite has been fabricated [61]. Figure 12 shows a schematic diagram of the fabrication process.

Melt Infiltration

Melt infiltration processing is another method to prepare dual-phase composites, particularly suitable for two components with large difference in melting points. Figure 13 shows a schematic illustration of the process, as in the case of a NiTi–W composite (articles in press). Melt infiltration method involves a molten metal being drawn by capillary forces or being pressurized into the pores of a preform, which is often the hard and high-melting-temperature component of the composite. In this case, the fluidity of the molten metal and its wettability to the preform metal are important for ensuring effective and complete infiltration. In general, fully densified composites are difficult to obtain by infiltration. In order to increase the density of final product, hot pressing is usually applied to the infiltrated composite after solidification. Using this method, a NiTi–W micro-fiber composite has been created. The W precursor used is metallic particulate W.

A NiTi–W Micro-Fiber Composite

The above part reviewed the design concept, objectives, and fabrication of SMA-enabled intermetallic composites. A novel NiTi–W micro-fiber composite was fabricated by means of melt infiltration and hot pressing.

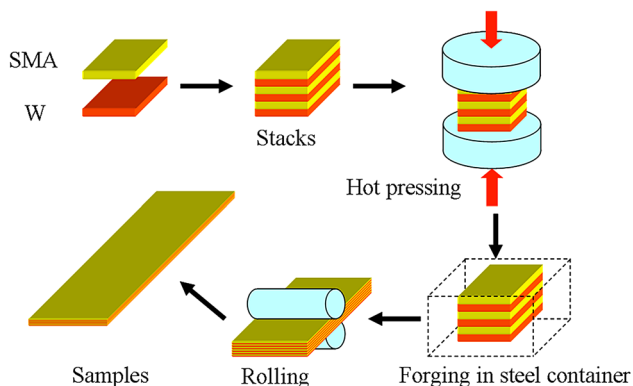


Fig. 12 Schematic of multilayer folding plate rolling process for fabricating ex situ SMA-enabled intermetallic composites

A W powder supplied by Zhuzhou Kete Industries Co., Ltd was used for this composite. The powder has an average particle size of 3 μm . The W powder was naturally filled in a graphite die to form the preform. A master alloy with nominal composition of $\text{Ti}_{53}\text{Ni}_{42}\text{Nb}_5$ (at.%) was prepared by vacuum induction melting for infiltration. Melt infiltration was performed at 1550 $^{\circ}\text{C}$ for 15 min in argon atmosphere in an induction furnace. The graphite die was then transferred into a vacuum hot pressing furnace with a graphite punch placed on the infiltrated sample. Hot pressing sintering was conducted at 1250 $^{\circ}\text{C}$ for 10 min under a uniaxial pressure of 30 MPa to densify the composite. The sintered composite was then sealed in a steel container and forged at 880 $^{\circ}\text{C}$ to a thickness of 6 mm. Finally, the forged composite was hot rolled multiple times into a sheet of 0.5 mm in thickness with intermediate anneals at 880 $^{\circ}\text{C}$ for 30 min. The forging and rolling processing reduced the W particles into micro-fibers.

Microstructure of the final composite product was observed using a FEI Quanta 200F scanning electron microscope (SEM). Differential scanning calorimetry (DSC) testing was conducted on a DSC TA Q20 instrument at a heating and cooling rate of 10 $^{\circ}\text{C}/\text{min}$. Tensile tests were conducted on a WDT II-20 testing machine equipped with an extensometer with a strain rate of $2 \times 10^{-4} \text{ s}^{-1}$ at room temperature. The samples for tensile testing were heat treated at 500 $^{\circ}\text{C}$ for 10 min. In situ synchrotron X-ray diffraction measurements were performed at the 11-ID-C beamline of the Advanced Photon Source at Argonne National Laboratory in the US. High-energy X-rays having a beam size of $0.8 \times 0.8 \text{ mm}^2$ and a wavelength of 0.117418 \AA were used to obtain two-dimensional (2-D) diffraction patterns in the transmission geometry. One-dimensional (1-D) HEXRD diffraction patterns under various applied strain were obtained by integrating along the specified azimuthal angle in the 2-D diffraction patterns using the FIT2D software package [66].

The composite exhibited reversible martensite transformation behavior under thermal cycles and could undergo stress-induced martensite transformation during tensile loading. The embedded W micro-fibers exhibited a high elastic strain up to 0.83% and the corresponding stress carried by W micro-fibers was evaluated as 3280 MPa, which is 1.5 times higher than monolithic bulk tungsten. The hot-rolled NiTi–W micro-fiber composite shows high tensile strength (2300 MPa) and appropriate plasticity (3.3%).

Figure 14 shows the microstructure of the NiTi–W composite. Figure 14a shows the microstructure after infiltration and pressure sintering. The bright spherules are W particles and the dark matrix is NiTi. The average size of the tungsten particles is about 7.8 μm , suggesting minor coarsening of the W particles during sintering. The volume

fraction of the tungsten particles is about 63.4%. No other intermetallics are found at the interface between W particles and the NiTi matrix. Figure 14b and c shows the microstructure of the composite after hot forging and hot rolling into a thin sheet at 880 °C. The tungsten particles have been converted into lamellar-like flat fibers, as shown in Fig. 14b (cross section) and c (longitudinal section). The

average dimensions of the flat W micro-fibers are about 0.6 μm in thickness, 5 μm in width, and 80 μm in length.

The martensitic transformation behavior of the NiTi matrix was analyzed by DSC, as shown in Fig. 15. The NiTi matrix exhibits a reversible $B2 \leftrightarrow B19'$ martensitic transformation at $M_s = 55^\circ\text{C}$. The alloy contains both B2-NiTi and B19'-NiTi at the room temperature.

Fig. 13 Schematic illustration of the fabrication procedure for NiTi–W composites by melt infiltration and hot pressing technique

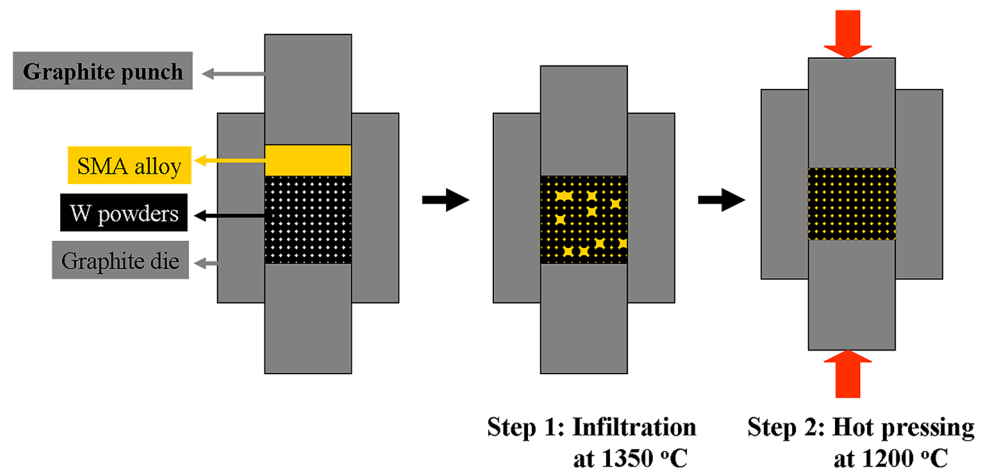
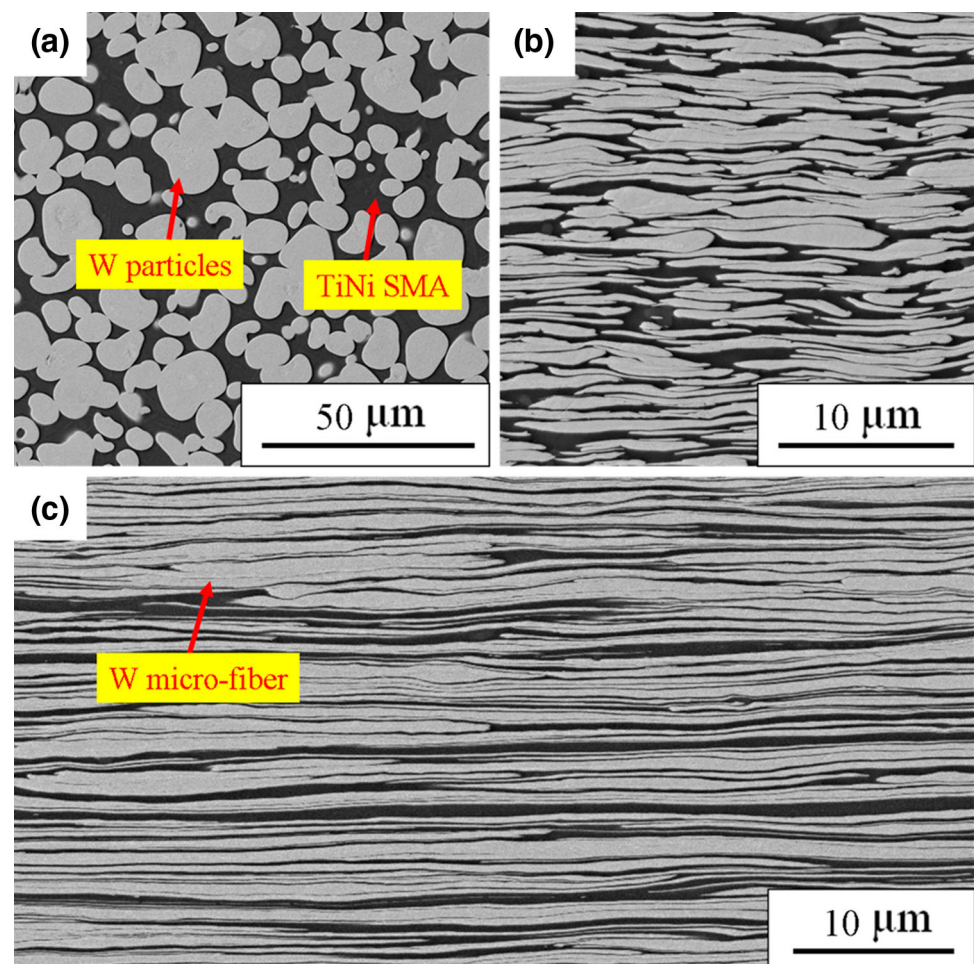


Fig. 14 Microstructures of the NiTi–W composite.

a Microstructure of the composite in the as-sintered state. **b** Microstructure of the composite in the final state after hot forging and hot rolling (cross-sectional view); **c** Microstructure of the composite in the final state after hot forging and hot rolling (longitudinal section view)



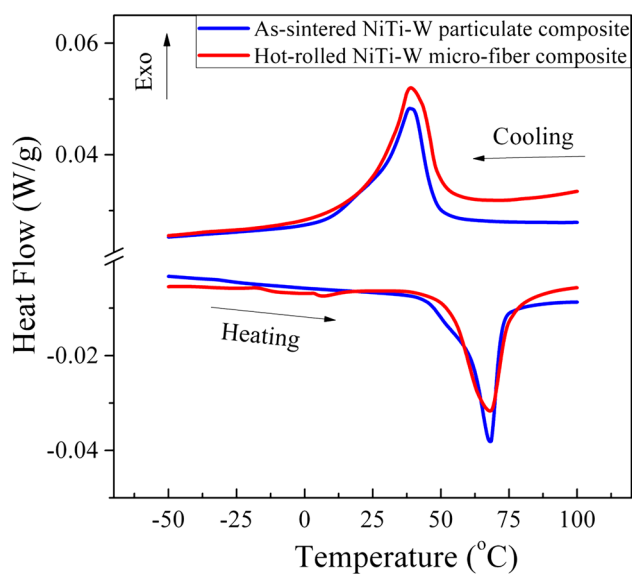


Fig. 15 DSC curves of the as-sintered NiTi–W particulate composite and the hot-rolled and annealed NiTi–W micro-fiber composite

Figure 16 shows two tensile deformation curves of the NiTi–W composite at room temperature. The NiTi–W particulate composite achieved in the as-sintered state exhibited a fracture strength of 1120 MPa and a fracture strain of 7.7%. The NiTi–W micro-fiber composite, formed after hot forging and hot rolling, had a yield strength of 1980 MPa, a fracture strength of 2300 MPa and a fracture strain of 3.3%. These properties are much higher than those of commercial hot-rolled tungsten plate products, typically 1700 MPa in fracture strength and 5.2% in fracture strain [67].

In situ high-energy synchrotron X-ray diffraction was performed to investigate deformation behavior of different phases in the composite during tensile deformation. Figure 17a shows the unrolled 2-D diffraction patterns at 0% applied strain (prior to deformation). The loading direction (also the rolling direction) is designated 90° in the azimuth circle. Both diffractions of the B2 phase (B2-(110)) and the B19' phase (B19'-(111) and B19'-(020)) are clearly present in the pattern, consistent with the prediction based on the DSC measurement. It is also evident that the diffraction intensities of NiTi and W are discontinuous and inhomogeneous around the azimuth circle, implying preferential orientation resulting from the hot rolling. When the applied strain was increased to 3.3%, as seen in Fig. 17b, the B19'-NiTi (111) and (020) diffractions intensify and the intensity of the B2-NiTi (110) diffraction diminishes, demonstrating the occurrence of the deformation-induced B2→B19' martensitic transformation. The W micro-fibers also show enhanced diffraction intensities in $\pm 45^\circ$ orientations for the W-(200) diffraction and $\pm 90^\circ$ orientations for the W-(110) diffraction, implying a strong [110] crystal texture along the rolling (and loading) direction.

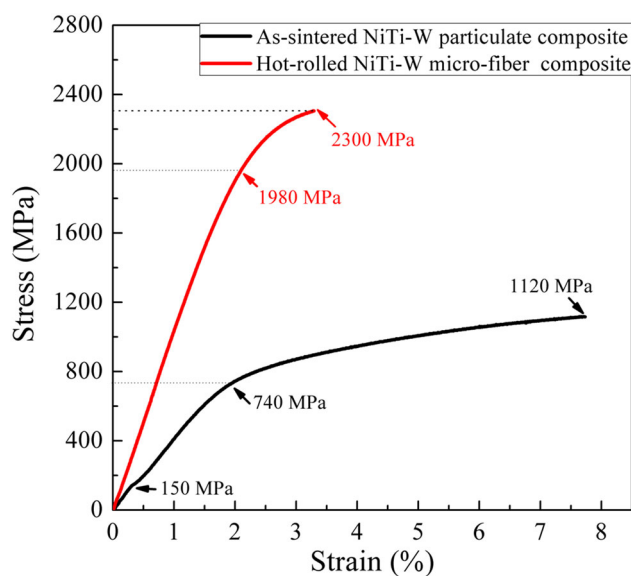


Fig. 16 Mechanical properties of the as-sintered NiTi–W particulate composite and the hot-rolled NiTi–W micro-fiber composite

Figure 18 shows 1-D synchrotron X-ray diffraction patterns of the composite taken in situ during tensile deformation. In these patterns, the peak position, which reflects lattice strain, can be determined. Figure 18a shows the W (110) diffraction peak, which is integrated from the 2-D patterns within the azimuthal angle range of 85° – 95° , i.e., along the loading direction. It is seen that with increasing applied strain, the W (110) diffraction peak shifts gradually to lower d-spacing values, as seen in Fig. 18a. The W (110) peak is also gradually broadened with increasing applied strain, due to increased lattice defect density. Figure 18b and c shows the diffraction peaks of the NiTi matrix, including both the B2 parent phase and the B19' martensite phase. The patterns are integrated from the 2-D patterns within the full azimuth circle of 0° – 360° . The peak positions of the diffractions of the NiTi matrix do not change but only their relative intensities, apparently due to the stress-induced B2→B19' transformation.

The lattice d-spacing strains of the W (110) planes normal to the loading direction (or strains along the loading direction) are determined from the 1-D XRD patterns, and plotted against the applied strain in Fig. 19a for both the as-sintered NiTi–W particulate composite and the hot-rolled NiTi–W micro-fiber composite. It is seen that the W (110) lattice d-spacing strain increased continuously with the increasing applied strain. The maximum lattice strain of the W particulate inclusions in the sintered composite reached 0.34 at 5% applied global strain. In comparison, the maximum lattice strain of the W micro-fiber inclusions in the hot-rolled composite reached 0.83 at 3.3% of the

Fig. 17 Synchrotron high-energy X-ray diffraction pattern of the hot-rolled NiTi–W micro-fiber composite, as presented in unrolled view along the 0–360° azimuthal angle. **a** At 0% applied strain; **b** At 3.3% applied strain. The tensile load is applied along 90°–270° direction, which is also the rolling direction of the sample, as indicated by the arrows

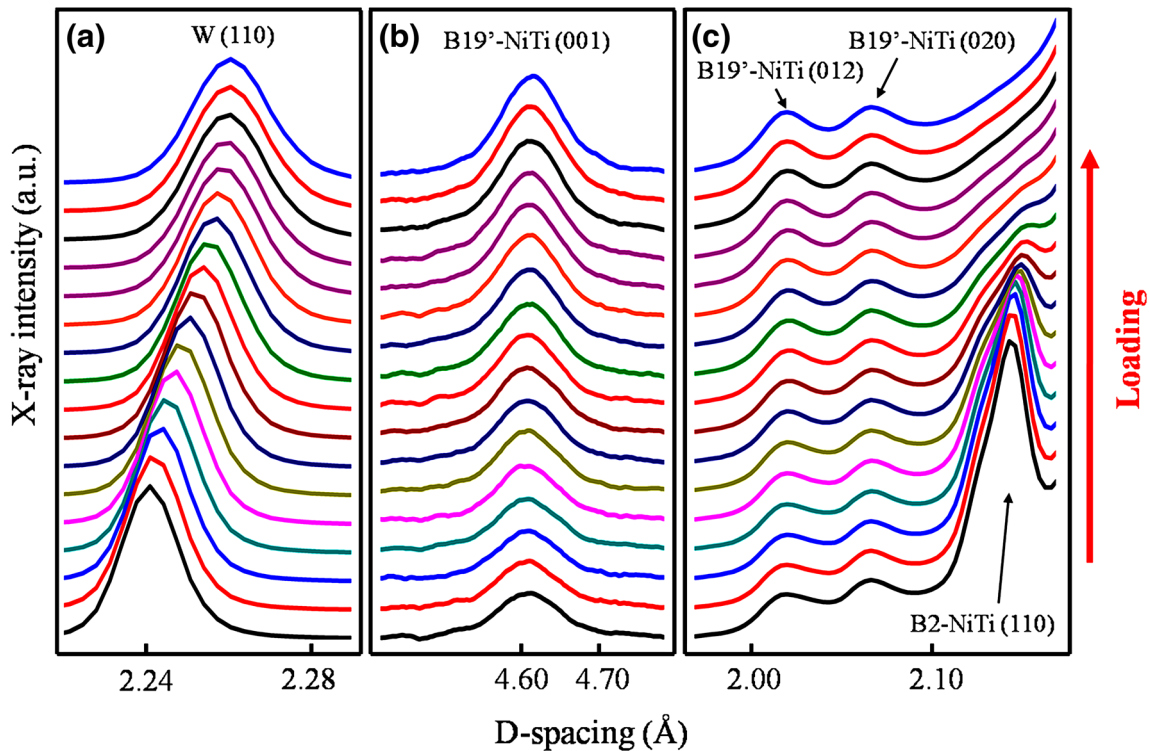
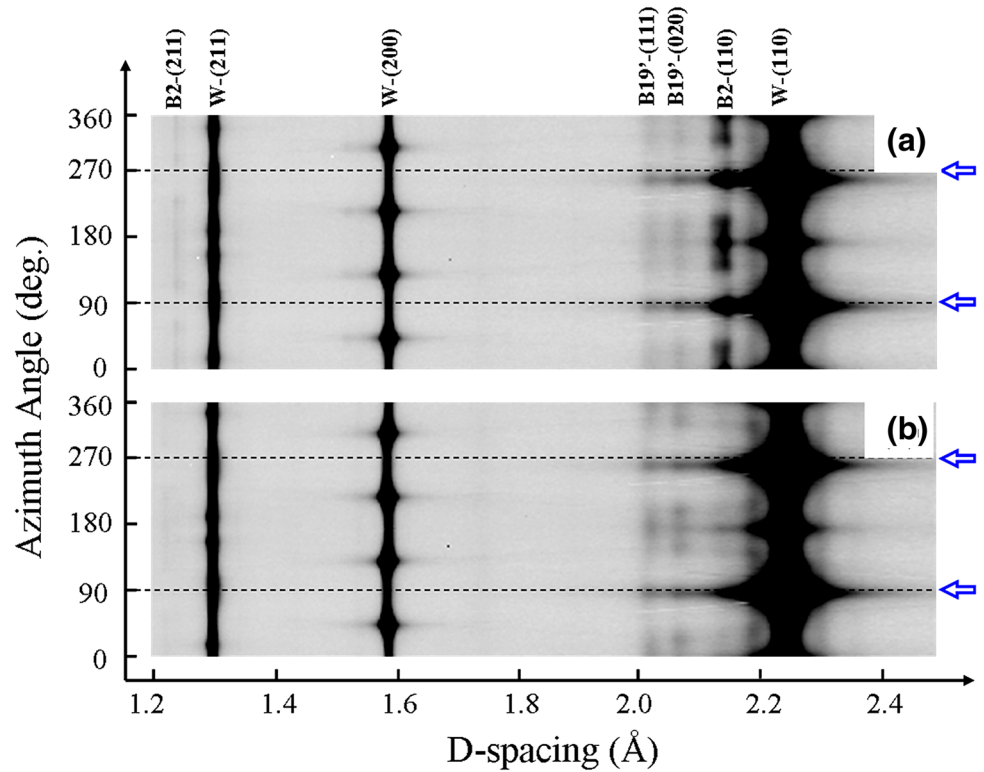
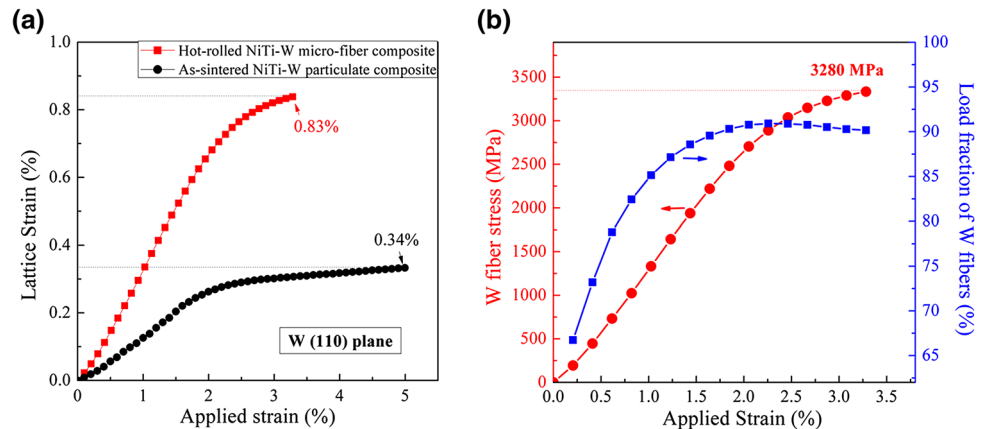


Fig. 18 1-D diffraction patterns of the hot-rolled NiTi–W micro-fiber composite extracted from the 2-D synchrotron X-ray diffraction patterns recorded in situ during tensile deformation at different levels of the applied strain. **a** W (110) diffraction peaks obtained by

integrating within 85°–95° azimuthal angle (i.e., along the loading direction); **b** and **c** B2 and B19'-NiTi diffraction peaks integrated within 0–360° azimuthal angle

Fig. 19 Analysis of elastic strains and lattice strains of W inclusions in the NiTi–W composite. **a** W (110) d-spacing strains in the loading direction as functions of the applied strain in the as-sintered NiTi–W particulate composite and the hot-rolled NiTi–W micro-fiber composite; **b** Stress and load fraction carried by the W micro-fibers as functions of the applied strain in the hot-rolled NiTi–W micro-fiber composite



applied strain, which is about 2.5 times of that of the W particulate inclusions.

The nominal stress carried by the W micro-fibers can be estimated using the elastic modulus of tungsten in [110] direction ($E_{W(110)}$), as $\sigma_W = E_{W(110)} \times \varepsilon_{W(110)}$, where $E_{W(110)} = 397$ GPa [68]. Then the load fraction carried by the W micro-fibers in the composite can be estimated by knowing their volume fraction ($f_W = 63.4\%$) as $\eta_W = \frac{\sigma_W \times f_W}{\sigma_W \times f_W + \sigma_{NiTi} \times f_{NiTi}} = \frac{\sigma_W \times f_W}{\sigma_{appl}}$, where σ_{appl} is the applied stress. The calculated values of σ_W and η_W are shown in Fig. 19b. It is seen that the W micro-fibers reached a maximum stress of 3280 MPa and with a volume fraction of 63.4% in the composite they carried 95% of the applied load at the end of the deformation. The maximum stress reached by the W micro-fibers is much higher than that of pure tungsten metal (~ 1900 MPa [67]). This demonstrates the natural high strength of the W micro-fibers and the effectiveness of load transfer from the NiTi matrix to the W micro-fibers due to the principle of lattice strain matching. The evidence shown in Fig. 19a also demonstrates that the lattice load transfer in the NiTi matrix is much more effective for the W micro-fibers than for the W particulates.

Conclusion Remarks

The principle of lattice strain matching between the SMA matrix and superelastic nanoinclusions has been used to fabricate novel SMA composite with exceptional properties. The shape memory behaviors are improved and super composites with exceptional mechanical properties have been created in different kinds of composites. A novel NiTi–W micro-fiber composite containing 63.4% W micro-fiber in volume fraction of this kind was fabricated by melt infiltration, hot pressing, forging, and hot rolling. The W micro-fiber reinforced composite exhibited a fracture tensile strength of 2300 MPa and a fracture strain of 3.3%. In situ synchrotron X-ray diffraction revealed that the NiTi

matrix underwent martensite transformation during tensile deformation. The maximum elastic strain of the W micro-fiber achieved was 0.83% in the loading direction, corresponding to a stress up to 3280 MPa, which carried 90% of load fraction during tensile deformation.

Acknowledgement This work was supported by the National Natural Science Foundation of China (NSFC) in Grant #51231008 (key program project scheme) and Grant #11474362, the Australian Research Council in Grant DP160105066. The use of the Advanced Photon Source was supported by the US Department of Energy, Office of Science, and Office of Basic Energy Science, Office of Basic Energy Sciences, under Contract No. DE-AC02-06CH11357.

References

- Köhl M, Bram M, Moser A, Buchkremer HP, Beck T, Stöver D (2011) Characterization of porous, net-shaped NiTi alloy regarding its damping and energy-absorbing capacity. *Mater Sci Eng A* 528:2454–2462
- Bansiddhi A, Sargeant TD, Stupp SI, Dunand DC (2008) Porous NiTi for bone implants: a review. *Acta Biomater* 4:773–782
- Zhao Y, Taya M, Kang Y, Kawasaki A (2005) Compression behavior of porous NiTi shape memory alloy. *Acta Mater* 53:337–343
- Grummon DS, Shaw JA, Foltz J (2006) Fabrication of cellular shape memory alloy materials by reactive eutectic brazing using niobium. *Mater Sci Eng A* 438–440:1113–1118
- Shaw JA, Grummon DS, Foltz J (2007) Superelastic NiTi honeycombs: fabrication and experiments. *Smart Mater Struct* 16:S170–S178
- Michailidis PA, Triantafyllidis N, Shaw JA, Grummon DS (2009) Superelasticity and stability of a shape memory alloy hexagonal honeycomb under in-plane compression. *Int J Solids Struct* 46:2724–2738
- Delobelle V, Delobelle P, Liu Y, Favier D, Louche H (2013) Resistance welding of NiTi shape memory alloy tubes. *J Mater Process Technol* 213:1139–1145
- Pilch J, Heller L, Sittner P (2009) Final thermomechanical treatment of thin NiTi filaments for textile applications by electric current
- Villa E, Arnaboldi S, Tuissi A, Giacomelli M, Turco E (2009) Mechanical analysis of hybrid textile composites with NiTi wires. *J Mater Eng Perform* 18:517–521
- Heller L, Vokoun D, Sittner P, Finckh H (2012) 3D flexible NiTi-braided elastomer composites for smart structure applications. *Smart Mater Struct* 21

11. Mahmud AS, Liu Y, Nam T-H (2008) Gradient anneal of functionally graded NiTi. *Smart Mater Struct* 17:015031
12. Mahmud AS, Liu Y, Nam TH (2007) Design of functionally graded NiTi by heat treatment. *Phys Scr T129*:222–226
13. Meng Q, Yang H, Liu Y, Nam T-H, Favier D (2013) Ti–50.8at.% Ni wire with variable mechanical properties created by spatial electrical resistance over-ageing. *J Alloys Compd* 577:S245–S250
14. Meng Q, Liu Y, Yang H, Nam T-H (2011) Laser annealing of functionally graded NiTi thin plate. *Scr Mater* 65:1109–1112
15. Meng Q, Liu Y, Yang H, Shariat BS, Nam T-H (2012) Functionally graded NiTi strips prepared by laser surface anneal. *Acta Mater* 60:1658–1668
16. Meng Q, Yang H, Liu Y, Nam T-H (2012) Compositionally graded NiTi plate prepared by diffusion annealing. *Scr Mater* 67:305–308
17. Shariat BS, Liu Y, Meng Q, Rio G (2013) Analytical modelling of functionally graded NiTi shape memory alloy plates under tensile loading and recovery of deformation upon heating. *Acta Mater* 61:3411–3421
18. Meng Q, Wu Z, Bakhtiari R, Shariat BS, Yang H, Liu Y, Nam T-H (2017) A unique “fishtail-like” four-way shape memory effect of compositionally graded NiTi. *Scr Mater* 127:84–87
19. Xiu Z, Laeng J, Sun X, Li Q, Hur SK, Liu Y (2008) Phase formation of Al₂O₃/Ti(C, N)–NiTi composite. *J Alloys Compd* 458:398–404
20. Strutt ER, Olevsky EA, Meyers MA (2008) Combustion synthesis/quasi-isostatic pressing of TiC–NiTi cermets: processing and mechanical response. *J Mater Sci* 43:6513–6526
21. Cheng F, Hu L, Reddy JN, Karaman I, Hoffman E, Radovic M (2014) Temperature-dependent thermal properties of a shape memory alloy/MAX phase composite: experiments and modeling. *Acta Mater* 68:267–278
22. Namli OC, Taya M (2011) Design of piezo-SMA composite for thermal energy harvester under fluctuating temperature. *J Appl Mech* 78:031001
23. Ni Q-Q, Zhang R-X, Natsuki T, Iwamoto M (2007) Stiffness and vibration characteristics of SMA/ER3 composites with shape memory alloy short fibers. *Compos Struct* 79:501–507
24. Kirkby EL, Michaud VJ, Månson JAE, Sottos NR, White SR (2009) Performance of self-healing epoxy with microencapsulated healing agent and shape memory alloy wires. *Polymer* 50:5533–5538
25. Lomas-González O, López-Cuellar E, López-Walle E, Araujo CJD, Reyes-Melo E, Gonzalez CH (2015) Thermomechanical behavior of a composite based on a NiTi ribbon with a magnetic hybrid polymer. *Mater Today* 2:S785–S788
26. Armstrong WD, Lorentzen T (1997) Fiber phase transformation and matrix plastic flow in a room temperature tensile strained NiTi shape memory alloy fiber reinforced 6082 aluminum matrix composite. *Scr Mater* 36:1037–1043
27. Coughlin JP, Williams JJ, Chawla N (2009) Mechanical behavior of NiTi shape memory alloy fiber reinforced Sn matrix “smart” composites. *J Mater Sci* 44:700–707
28. Esen Z (2012) The effect of processing routes on the structure and properties of magnesium–TiNi composites. *Mater Sci Eng A* 558:632–640
29. Aydogmus T (2015) Processing of interpenetrating Mg–TiNi composites by spark plasma sintering. *Mater Sci Eng A* 624:261–270
30. Coughlin JP, Williams JJ, Crawford GA, Chawla N (2008) Interfacial reactions in model NiTi shape memory alloy fiber-reinforced Sn matrix “Smart” composites. *Metall Mater Trans A* 40:176–184
31. Kuang KSC, Cantwell WJ (2003) The use of plastic optical fibres and shape memory alloys for damage assessment and damping control in composite materials. *Meas Sci Technol* 14:1305
32. Cortes P, Terzak J, Kubas G, Phillips D, Baur JW (2014) The morphing properties of a vascular shape memory composite. *Smart Mater Struct* 23:015018
33. Hao S, Cui L, Jiang D, Han X, Ren Y, Jiang J, Liu Y, Liu Z, Mao S, Wang Y, Li Y, Ren X, Ding X, Wang S, Yu C, Shi X, Du M, Yang F, Zheng Y, Zhang Z, Li X, Brown DE, Li J (2013) A transforming metal nanocomposite with large elastic strain, low modulus, and high strength. *Science* 339:1191–1194
34. Yang F, Ni D, Hao S, Li S, Ma Z, Liu Y, Feng C, Cui L (2015) Microstructure and phase stress partition of Mo fiber reinforced CuZnAl composite. *Mater Sci Eng A* 628:419–422
35. Hao S, Cui L, Wang H, Jiang D, Liu Y, Yan J, Ren Y, Han X, Brown DE, Li J (2016) Retaining large and adjustable elastic strains of kilogram-scale Nb nanowires. *ACS Appl Mater Interfaces* 8:2917–2922
36. Li GF, Zheng HZ, Shu XY, Peng P (2015) Structural stability of characteristic interface for NiTi/Nb nanowire: first-principle study. *Met Mater Int* 22:69–74
37. Zang K, Mao S, Cai J, Liu Y, Li H, Hao S, Jiang D, Cui L (2015) Revealing ultralarge and localized elastic lattice strains in Nb nanowires embedded in NiTi matrix. *Sci Rep* 5:17530
38. Li J, Shan Z, Ma E (2014) Elastic strain engineering for unprecedented materials properties. *MRS Bull* 39:108–114
39. Schlom DG, Chen L-Q, Fennie CJ, Gopalan V, Muller DA, Pan X, Ramesh R, Uecker R (2014) Elastic strain engineering of ferroic oxides. *MRS Bull* 39:118–130
40. Yildiz B (2014) “Stretching” the energy landscape of oxides—effects on electrocatalysis and diffusion. *MRS Bull* 39:147–156
41. Bedell SW, Khakifirooz A, Sadana DK (2014) Strain scaling for CMOS. *MRS Bull* 39:131–137
42. Zhang J, Liu Y, Ren Y, Huan Y, Hao S, Yu C, Shao Y, Ru Y, Jiang D, Cui L (2014) In situ synchrotron X-ray diffraction study of deformation behavior and load transfer in a Ti₂Ni–NiTi composite. *Appl Phys Lett* 105:041910
43. Yu C, Liu Z, Liu Y, Shao Y, Ren Y, Cui L (2016) Load transfer in phase transforming matrix–nanowire composite revealing the significant load carrying capacity of the nanowires. *Mater Des* 89:721–726
44. Yue Y, Liu P, Zhang Z, Han X, Ma E (2011) Approaching the theoretical elastic strain limit in copper nanowires. *Nano Lett* 11:3151–3155
45. Wu B, Heidelberg A, Boland JJ (2005) Mechanical properties of ultrahigh-strength gold nanowires. *Nat Mater* 4:525–529
46. Richter G, Hillerich K, Gianola DS, Monig R, Kraft O, Volkert CA (2009) Ultrahigh strength single crystalline nanowhiskers grown by physical vapor deposition. *Nano Lett* 9:3048–3052
47. Zhu T, Li J (2010) Ultra-strength materials. *Prog Mater Sci* 55:710–757
48. Otsuka K, Ren X (2005) Physical metallurgy of Ti–Ni-based shape memory alloys. *Prog Mater Sci* 50:511–678
49. Mohd Jani J, Leary M, Subic A, Gibson MA (2014) A review of shape memory alloy research, applications and opportunities. *Mater Des* 56:1078–1113
50. Ogata S, Li J, Yip S (2002) Ideal pure shear strength of aluminum and copper. *Science* 298:807–811
51. Thilly L, Petegem SV, Renault P-O, Lecouturier F, Vidal V, Schmitt B, Swygenhoven HV (2009) A new criterion for elasto-plastic transition in nanomaterials: application to size and composite effects on Cu–Nb nanocomposite wires. *Acta Mater* 57:3157–3169
52. Zhang J, Cui L, Jiang D, Liu Y, Hao S, Ren Y, Han X, Liu Z, Wang Y, Yu C, Huan Y, Zhao X, Zheng Y, Xu H, Ren X, Li X (2015) A biopolymer-like metal enabled hybrid material with exceptional mechanical prowess. *Sci Rep* 5:8357
53. Sun QP, He YJ (2008) A multiscale continuum model of the grain-size dependence of the stress hysteresis in shape memory alloy polycrystals. *Int J Solids Struct* 45:3868–3896

54. Kim Y-H, Cho G-B, Hur S-G, Jeong S-S, Nam T-H (2006) Nanocrystallization of a Ti–50.0Ni(at.%) alloy by cold working and stress/strain behavior. *Mater Sci Eng A* 438–440:531–535
55. Hao S, Cui L, Jiang D, Yu C, Jiang J, Shi X, Liu Z, Wang S, Wang Y, Brown DE, Ren Y (2013) Nanostructured Nb reinforced NiTi shape memory alloy composite with high strength and narrow hysteresis. *Appl Phys Lett* 102:231905
56. Jiang D, Hao S, Zhang J, Liu Y, Ren Y, Cui L (2014) In situ synchrotron investigation of the deformation behavior of nanolamellar Ti₅Si₃/TiNi composite. *Scr Mater* 78–79:53–56
57. Hao SJ, Cui LS, Wang YD, Jiang DQ, Yu C, Jiang J, Brown DE, Ren Y (2011) The ultrahigh mechanical energy-absorption capability evidenced in a high-strength NbTi/NiTi nanocomposite. *Appl Phys Lett* 99:024102
58. Wang S, Cui L, Hao S, Jiang D, Liu Y, Liu Z, Mao S, Han X, Ren Y (2014) Locality and rapidity of the ultra-large elastic deformation of Nb nanowires in a NiTi phase-transforming matrix. *Sci Rep* 4:6753
59. Jiang D, Liu Y, Yu C, Liu W, Yang H, Jiang X, Ren Y, Cui L (2015) Deformation behavior of Nb nanowires in TiNiCu shape memory alloy matrix. *Mater Sci Eng A* 646:52–56
60. Wang S, Guo FM, Jiang DQ, Liu Y, Cui LS (2014) In situ W-NiTi shape memory alloy composite of high radiopacity. *Scr Mater* 81:4–7
61. Shao Y, Yu K, Jiang D, Yu C, Ren Y, Jiang X, Guo F, Cui L (2016) High strength W/TiNi micro-laminated composite with transformation-mediated ductility. *Mater Des* 106:415–419
62. Piao M, Miyazaki S, Otsuka K, Nishida N (1992) Effects of Nb addition on the microstructure of Ti–Ni alloys. *Mater Trans JIM* 33:337–345
63. Luo W, Ishikawa K, Aoki K (2008) Hydrogen permeable Ta–Ti–Ni duplex phase alloys with high resistance to hydrogen embrittlement. *J Alloys Compd* 460:353–356
64. Song G, Dolan MD, Kellam ME, Liang D, Zambelli S (2011) V–Ni–Ti multi-phase alloy membranes for hydrogen purification. *J Alloys Compd* 509:9322–9328
65. Zhang H, He Y, Yang F, Liu H, Jin Z (2013) Thermodynamic assessment of Cu–Ni–Ti ternary system assisted with key measurements. *Thermochim Acta* 574:121–132
66. Hammersley AP, Svensson SO, Hanfland M, Fitch AN, Hausermann D (1996) Two-dimensional detector software: from real detector to idealised image or two-theta scan. *High Press Res* 14:235–248
67. Wei Q, Kecskes LJ (2008) Effect of low-temperature rolling on the tensile behavior of commercially pure tungsten. *Mater Sci Eng A* 491:62–69
68. Ma B, Rao Q-H, He Y-H (2014) Effect of crystal orientation on tensile mechanical properties of single-crystal tungsten nanowire. *Trans Nonferr Met Soc* 24:2904–2910